Delft University of Technology

A Novel Composite Sensor for UHF Partial Discharge and Gas State Measurement in GIS

Chen, Huan; Zhang, Zhaoyu ; Guo, Ruochen; Han, Xutao ; Zhang, Xuanrui ; Lin, Junhao

Important note
To cite this publication, please use the final published version (if applicable).
Please check the document version above.

A Novel Composite Sensor for UHF Partial Discharge and Gas State Measurement in GIS

Huan Chen⬚, Haotian Wang⬚, Zhaoyu Zhang⬚, Ruochen Guo⬚, *Member, IEEE*, Xutao Han⬚, Xuanrui Zhang⬚, and Junhao Li⬚, *Senior Member, IEEE*

Abstract— The gas state of the insulating gas significantly impacts the development and extent of the partial discharge (PD) in gas-insulated switchgear (GIS). Correlating these two factors allows for a more comprehensive diagnosis of insulation defects. At present, the ultrahigh-frequency (UHF) method has been widely used for PD detection in GIS. However, the measurements of the insulating gas's state in the field are primarily conducted offline or at gas valves, providing ineffective data for reference. To address this challenge, this article introduces a novel composite sensor capable of simultaneous UHF and gas state measurements. Building upon the disk-type UHF sensor structure, the composite sensor integrates a gas state sensing unit with the micro-electromechanical systems (MEMS) sensor as the core. A robust shielding shell is designed through finite element simulation to ensure the safety of the sensor, with the maximum induced voltage and electric field strength on the sensing unit measuring 0.28 V and 414 V/m, respectively. The average UHF measurement sensitivity of the composite sensor reaches 13.3 mm. In addition, the composite sensor exhibits low errors (± 0.2 °C, ± 3 kPa, and ± 10 μL/L), high consistency and repeatability in temperature, pressure, and moisture measurement. Finally, the composite sensor has demonstrated its capability to simultaneously and safely detect PD signals and the gas state within GIS.

Index Terms— Combined detection, electromagnetic shielding, gas-insulated switchgear (GIS), gas state, micro-electromechanical systems (MEMS) sensor, ultrahigh frequency (UHF).

I. INTRODUCTION

WITH the advantages of a compact structure, minimal land usage, and ease of maintenance, gas-insulated switchgear (GIS) has been widely adopted in the power grid. However, during manufacturing, transportation, field assembly, and operation, GIS inevitably has insulation defects. Partial discharge (PD) will occur preferentially at these insulation defects, exacerbating insulation degradation and eventually leading to breakdown that jeopardize the safety of the power system. Various PD measurement methods, including acoustic, optical, electrical, and magnetic, have been extensively employed for diagnosing insulation defects. Nonetheless, the field operation experience shows that the current diagnostic methods still miss and misjudge the insulation defects [1], [2]. Actually, as the centerpiece of equipment insulation, the insulating gas is closely related to the PD, significantly influencing the development and extent of PD development [3], [4], [5], [6]. Therefore, it is necessary to simultaneously detect the insulating gas's state and the PD inside the GIS for correlation analysis, enabling a more precise diagnosis of insulation defects.

Among various PD detection methods, ultrahigh-frequency (UHF) measurement method is widely used due to its high sensitivity and anti-interference ability, and the UHF sensor has seen the mature development after years [7]. UHF sensors are also used as a base structure in combination with other types of sensors for combined detection: UHF-optical composite sensor [8] and UHF-overvoltage composite sensor [9].

In the field, density relays connected to the GIS though a tee valve are typically used to measure the gas state, triggering alerts or lockouts when the density falls below a preset value. There are two types of density relays used: mechanical and electronic. Values measured by mechanical relays need manual periodic recording, while electronic density relays generally derive density by measuring pressure and gas temperature [10], [11], [12]. Direct measurement of temperature distribution inside GIS chamber is challenging. It is typically inferred by periodic infrared imaging or online monitoring of shell temperature using thermometric resistance [13], [14], [15]. Dew point meters based on the cold mirror principle measure moisture content quite accurately, but they are bulky and require extraction of a certain volume of insulating gas during measurement. Online capacitive dew point meters can only be installed at the tee valve [16], [17], [18]. The aforementioned detection methods are either offline testing or single-parameter detection, lacking the capability for integrated analysis. With the advancement of smart substations, some gas state online monitoring devices based on multiple sensors have emerged in recent years, enabling the detection of multiple gas state parameters [19], [20]. However, these devices are still installed at the tee valve position, and gas temperature is typically recorded, where the devices are installed. Due to heat flux, this can impact the actual measured values, potentially misleading insulation status judgments [21], [22].

Internal detection using multisensors is considered a preferable solution, but safely incorporating secondary-side sensors

internally has posed a challenge. Optical fiber has been installed within GIS to collect information, such as temperature, PD, and decomposed gases. This approach is advantageous because it represents a nonelectrical detection method with excellent electromagnetic immunity [23], [24], [25]. However, internal sensors capable of detecting pressure and moisture using nonelectrical means have not yet been developed. Luckily, active electronic transformers are a good reference for internal charged detection after reliable shielding [26], [27]. Meanwhile, with the rapid development of micro-electromechanical systems (MEMS), MEMS sensors have gained widespread use in automation equipment owing to their small size, high sensitivity, low power consumption, and capacity for multiparameter sensing [28], [29], [30]. Leveraging the benefits of MEMS sensors, the internal detection of MEMS sensors is not impossible to be realized as long as the shielding design is reliable.

In this article, a gas state sensing unit integrated with MEMS sensors is first designed, achieving the combination of gas state parameter acquisition, simultaneous processing, and transmission functions. The unit is capable of simultaneously measuring gas state parameters, including temperature, pressure, density, moisture content, and dew point and so on. Then, based on the proven UHF sensor structure, a reliable electromagnetic shielding shell is designed using finite element calculations to realize the internal detection of the gas state sensing unit. In previous study [31], it has been concluded that the temperature distribution inside the GIS can be inverted by the internal and external temperatures, while distribution of the density and moisture depends on this temperature field [32] Therefore, when the composite sensor measures the PD signals, the gas state data measured by the composite sensor at the same time can be inverted to the gas state distribution of the whole cavity of the GIS, thus providing an effective reference for the joint diagnosis of insulation defects. Finally, it is experimentally demonstrated that the composite sensor performs outstandingly in UHF and gas state measurements, meeting the measurement requirements of the corresponding parameters within the GIS. It is the first time MEMS sensors will be used for gas detection equipment built directly into the GIS cavity, which will provide a design foundation for other types of sensors to be built in the future.

This article is organized as follows. Section II first introduces the overall structure of the composite sensor and the circuit and algorithm design of the gas state sensing unit. Section III incrementally advances the electromagnetic shielding design of the composite sensor through simulation techniques to ensure the safety of the embedded gas state sensing unit. Section IV describes the performance of each part of the composite sensor, followed by experimental validation of the safety and practical application effectiveness of the composite sensor.

II. Overall Design of the Composite Sensor

A. Overview of the Composite Sensor

The developed composite sensor can be easily installed directly at the GIS flange, allowing for simultaneous measurement of UHF signals excited by PD, as well as temperature,
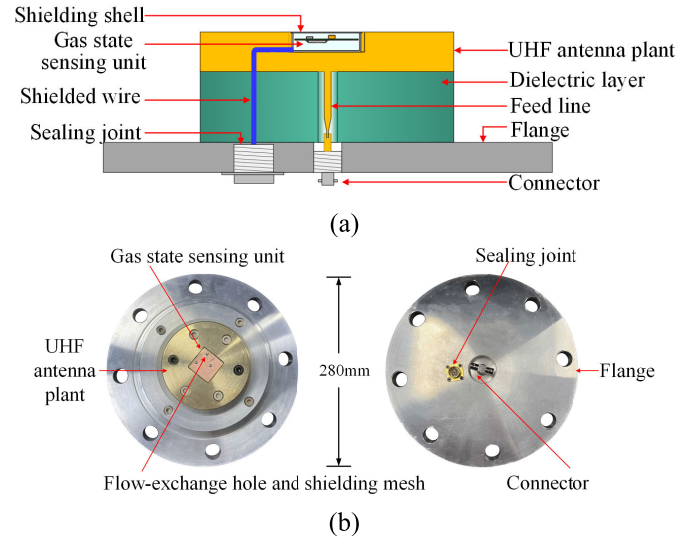

Fig. 1.   Composite sensor. (a) Structural profile. (b) Physical diagram.

pressure, and moisture content state of the insulating gas. The structural profile and physical diagram of the composite sensor is shown in Fig. 1.

Due to its simple structure, high sensitivity, and minimal impact on the electric field within the GIS, the disk-type antenna is widely employed as the internal UHF sensor for PD monitoring. As depicted in Fig. 1(a), the basic structure of the UHF sensor consists of a copper UHF antenna plate at the top, a dielectric layer in the middle, the flange at the bottom, and a feed line. The UHF antenna is capable of receiving electromagnetic waves excited by the PD and transmitting the induced voltage to the outside via the feed line and connector.

Based on the UHF sensor's structure, a gas state sensing unit is embedded within the UHF antenna plate, encased by a grounded shielding shell composed of high magnetic permeability and high electrical conductivity material. The gas state sensing unit employs MEMS sensors as its core component and integrates microcontroller unit (MCU), electromagnetic compatibility (EMC), and other devices, enabling the collection, processing, and transmission of gas state data. Directly above the MEMS sensor on the gas state sensing unit, a flow-exchange hole is machined into the shielding shell for gas exchange between the inside and outside, particularly for moisture content. A shielding mesh covers the upper part of the flow-exchange hole to further enhance the shielding function. The data collected by the gas state sensing unit is processed by the MCU and then transmitted via a six-core ultrafine shielded cable. A cable routing channel is machined within the UHF sensor to accommodate the ultrafine shielded cable, and a glass sintered sealing joint is attached to the bottom flange to ensure both hermetic sealing and data transmission.

B. Circuit Design of the Gas State Sensing Unit

The circuit structure of the gas state sensing unit is depicted in Fig. 2(a), consisting a two-layer circuit board with an overall size of $25 \times 25 \times 7$ (mm^3). The parameters of key components are detailed in Table I. Since the gas sensors require full contact with the gas for obtaining gas state data, while the other components do not, only two MEMS sensors
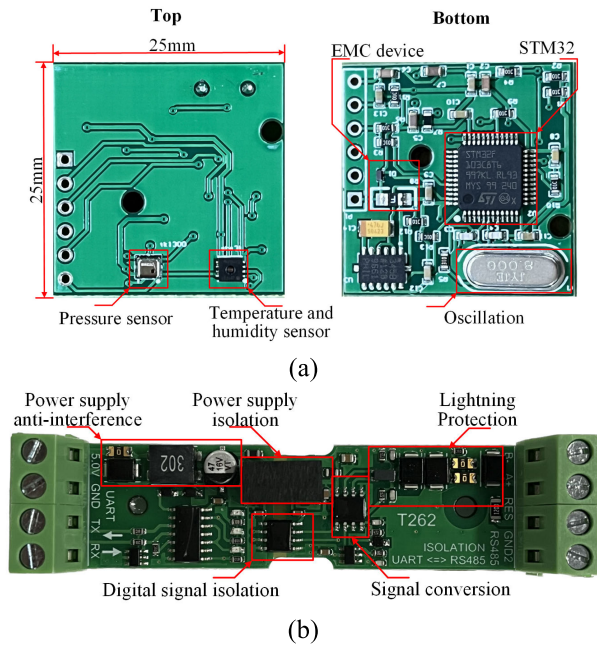
Fig. 2. Circuit structure. (a) Gas state sensing unit. (b) Converter.

TABLE I
PARAMETERS OF THE KEY COMPONENTS

Device	Parameter	Others
Temperature and humidity sensor	Measuring range: -40~125 °C and 0~100% RH Typical accuracy: ±2% RH and ±0.3 °C	IIC Interface Package size: 2.5×2.5×0.9(mm³)
Pressure sensor	Operating range: -40~85 °C Measuring range: 0~1000KPa Typical accuracy: ±10KPa	1-Wire Bus Package size: 2.3×2.6×1.45(mm³)
MCU	Operating range: -40~85 °C Cortex-M3 Core, 32 Bit, 64kB Flash, 48-LQFP, 72MHz Frequency, IIC, 1-Wire, UART	
Transient Voltage Suppressors (TVS)	Reverse stand-off voltage: ±4.6V Max Electrostatic discharge: ±30kV (contact and air) Electrical Fast Transients: 40A (5/50ns)	
Resettable Fuse (PTC)	Self-recovery type, Trip Current: 2.2A Time to Trip: 0.3s	

are positioned on the top of the sensing unit. On the reverse side, there are MCU, an external high-speed crystal oscillator, EMC devices, along with essential resistors and capacitors forming the circuit.

To streamline the shielding design work and preserve the performance of the UHF antenna following the integration of the sensing unit, it is crucial to keep the sensing unit as compact as possible. Hence, MEMS sensors are selected as the central component for measurements. Additionally, as there is not a MEMS sensor capable of directly detecting trace moisture currently, relative humidity (RH) measurements were employed as an indirect means to ascertain trace moisture content.

An STM32F103C8T6 [33] is adopted as the MCU. Its extensive general-purpose input–output (GPIO) ports can meet

the connection with MEMS sensors and external host computer. Furthermore, the external 8-MHz high-speed crystal oscillator ensures the provision of precise clock signals, thereby enabling stable program operation, even when exposed to electromagnetic interference.

The gas state sensing unit is linked to the external system through a mere six wires, assigned roles in powering, communication, and grounding the unit. Additionally, four of these wires can be utilized for program copying, simplifying the internal calibration of the sensing unit during prolonged operation. The power supply passes through the EMC device before supplying each part, and both the MEMS sensors and MCU feature integrated EMC structures, thus ensuring the basic electromagnetic compatibility of the gas sensing unit.

The MCU transmits the gathered gas state data from inside the GIS to the outside through the universal asynchronous receiver/transmitter (UART) bus, subsequently sending them to a nearby data summary cabinet. From there, the data are uploaded to the cloud via the substation Internet of Things and are ultimately displayed in real time within the substation control room. However, the UART bus method lacks the capability to resist interference over long distances. To address this, a conversion circuit, as shown in Fig. 2(b), has been designed to convert it to the RS-485 bus. This conversion circuit is powered by an external 5-V lithium battery. The power supply anti-interference measures to safeguard the circuit against overvoltage, overcurrent, and common mode interference signals from the power supply end. The UART signal is entirely isolated from the RS-485 signal, achieved through power supply isolation via a dc–dc module and digital signal isolation via a magnetic coupling module. Once isolated, there is no interference between the external line and the internal sensor, ensuring that a failure at one end will not cause secondary damage to the other part. Following the signal converter, there is a series of lightning protection components capable of rapidly discharging surge voltage in the event of a lightning strike on the external line and clamping the voltage on the converter module at a low level.

The data exchange format between the sensing unit and the data summary cabinet adopts MODBUS-RTU communication protocol, which follows a master/slave architecture. In the RS-485 network, the data summary cabinet functions as a master node, while the other gas state sensing units act as slave nodes. Each gas state sensing unit possesses a unique address, allowing the host to communicate with the respective sensing unit by issuing distinct address commands to access gas state information from various installation locations.

C. Algorithms for Gas State Data Processing

The temperature (t, in °C), pressure (P), and RH of the insulating gas are measured directly by the two MEMS sensor, but they are insufficient. Therefore, the following processes are employed to obtain additional parameters based on these three gas state parameters.

When t is acquired, saturated water vapor pressure (e_{sw}) at this specific temperature can be calculated according to IEEE C37.122.5 [34].

Equation (1) is valid with respect to ice in the range −60 °C–0 °C

$$e_{\text{sw}} = 611.2 \times \exp\left(\frac{22.46 \times t}{272.62 + t}\right). \tag{1}$$

Equation (2) is valid for temperatures 0 °C to +50 °C.

$$e_{\text{sw}} = 611.2 \times \exp\left(\frac{17.62 \times t}{243.12 + t}\right). \tag{2}$$

The calculation formula is not applicable when the temperature exceeds 50 °C, but e_{sw} at various temperatures is provided in the standard [35]. In the processing program, a pre-established 2-D matrix concerning the temperature is used, allowing for the retrieval of e_{sw} values above 50 °C by referencing the matrix.

The water vapor partial pressure (e) is determined by (3). Subsequently, the dew point temperature (t_d) can be calculated by substituting the water vapor partial pressure into (1) and (2)

$$\text{RH}(\%) = \frac{e}{e_{\text{sw}}} \times 100\%. \tag{3}$$

The moisture content (ppm_v, in μL/L) can be calculated through the following equation:

$$\text{ppm}_v = \frac{e}{P - e} \times 10^6. \tag{4}$$

Using the Beattie–Bridgeman equation of state [36], as described in (5), gas density (ρ, in kg/m^3) can be derived based on the values of T and P

$$
\begin{aligned}
P &= (\text{RT}B - A)\rho^2 + \text{RT}\rho \\
A &= 73.882 - 5.132105 \times 10^{-2}\rho \\
B &= 2.50695 \times 10^{-3} - 2.12283 \times 10^{-6}\rho \\
R &= 56.9502
\end{aligned} \tag{5}
$$

where T is the thermodynamic temperature in K.

To facilitate comparison, it is necessary to convert all parameters into standard parameters, including pressure P_{20} at 20 °C, moisture content ppm_{v20} at 20 °C, and dew point t_{d1} at 1 atm. This is achieved by substituting the previous calculated density and standard temperature of 20 °C into (5) to obtain P_{20}, and then, ppm_{v20} can be calculated by (6) [37]. t_{d1} is determined by calculating the water vapor pressure to 1 atm and then substituting it back

$$\text{ppm}_{v20} = \frac{e_{\text{sw}20}}{e_{\text{sw}}} \times \frac{P}{P_{20}} \times \text{ppm}_v. \tag{6}$$

In summary, ρ, t_d, ppm_v, P_{20}, ppm_{v20}, and t_{d1} were derived indirectly from direct measurement of t, RH, and P, resulting in a total of nine parameters.

III. ELECTROMAGNETIC SHIELDING

Being a low-voltage unit, the gas state sensing unit is inevitably exposed to the potent electromagnetic field within high-voltage GIS once integrated. In order to make clear the electric field, magnetic field, and induced voltage that the gas state sensing unit is subjected to, and to make a targeted shielding design, a 1:1 overall modeling of the GIS and composite sensor is conducted in the finite element simulation
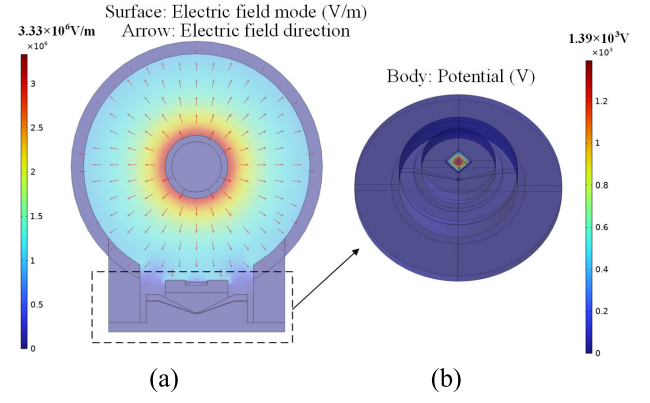

Fig. 3. Electric field simulation results. (a) Internal electric field distribution. (b) Induced potential distribution on the composite sensor.
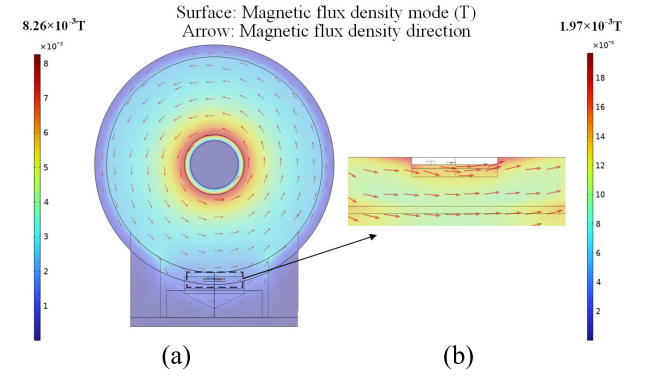

Fig. 4. Magnetic field simulation results. (a) Internal magnetic field distribution. (b) Magnetic field distribution on the composite sensor.

software. In the modeling process, any structures that do not affect the simulation results are simply omitted. Aluminum is chosen as the material for all metallic parts expect UHF antenna plate, which is made of copper. The materials of dielectric layer, circuit board, and MEMS sensors are poly tetra fluoroethylene (PTFE), epoxy glass cloth (FR-4), and silicon, respectively. The SF$_6$ is filled in the GIS cavity. The maximum field is mainly investigated; hence, the simulation is not time dependent. The enclosure is grounded and the gas state sensing unit is set to a suspended potential. The electrostatic and magnetic field modules are utilized to solve for the electric field, magnetic field, and potential distributions of the GIS when the conductor is applied with rated voltage and rated industrial frequency current, respectively.

A. Electromagnetic Field Without Shield

Taking 330-kV GIS as an example, without any shielding measures, the simulation results are depicted in Figs. 3 and 4. In Fig. 3(a), it is evident that the electric field inside the GIS exhibits a divergent pattern, with the electric field intensity decreasing uniformly from the inner conductor to the grounded enclosure and the electric field lines pointing toward the enclosure. At the position of the composite sensor, the electric field lines are perpendicular to the gas state sensing unit. The maximum electric field generated by 330-kV GIS can reach 3.33×10^6 V/m. Further observation of the induced voltage on the composite sensor in Fig. 3(b) reveals that
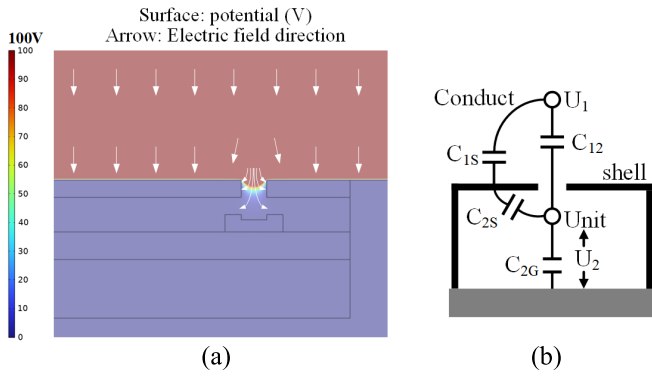
Fig. 5. Electric field shielding effect. (a) Simulation result. (b) Equivalent distributed parameter circuit model.

the induced voltage on the gas state sensing unit is as high as 1.39 kV. In the absence of any shielding, the gas state sensing unit is bound to be broken down. The magnetic field distribution is demonstrated in Fig. 4(a), where the magnetic field exhibits a spiral shape around the inner conductor, and the magnetic flux density decreases from inside to outside. At the position of the composite sensor in Fig. 4(b), the magnetic field lines are nearly parallel to the gas state sensing unit. The maximum magnetic flux density of 330-kV GIS under the rated 2000-A power frequency current is only 8.26×10^{-3} T, mainly because most of the materials inside the GIS are poor magnetic conductors with high magnetic resistance.

From the above analysis, it can be seen that direct installation of the composite sensor without shielding measures is unsafe, so it is necessary to undertake electromagnetic shielding design.

B. Design of the Electric Field Shielding

To guarantee the safety of the gas state sensing unit after implantation, a shielding shell constructed from a material possessing excellent electrical conductivity is devised, and it is grounded securely. The higher conductivity is to further enhance its grounding reliability. Additionally, a flow-exchange hole is opened in the shielding shell directly above the temperature and humidity MEMS sensor only. The initial size of the flow-exchange hole is designed at 1.5 mm, corresponding to the sensing hole of 1.5 mm in the MEMS sensor. This design scheme is modeled accordingly in the finite element software, and the simulation results are presented in Fig. 5(a).

From a field perspective analysis, the grounded shielding shell intercepts the majority of electric field lines that originally point vertically to the gas state sensing unit, redirecting them to terminate on the shell itself. This greatly reduces the field intensity and induced voltage on the sensing unit. However, some field lines still pass through the flow-exchange hole, subjecting the MEMS sensor to a residual electric field that can produce a nonnegligible induced voltage.

Analyzing from the perspective of the circuit, each part of the device is characterized by distribution parameters, as shown in Fig. 5(b). Without any shielding measure, there is a direct coupling between the conductor and the gas state

sensing unit, creating a high-voltage arm capacitance denoted as C_{12}, and the coupling between the sensing unit and the ground generates the low-voltage arm capacitance labeled as C_{2G}. According to the capacitance divider principle, the induced voltage on the gas state sensing unit can be expressed as follows:

$$U_2 = \frac{U_1 C_{12}}{C_{12} + C_{2G}}. \tag{7}$$

After applying the shielding shell, the original coupling capacitance of the high-voltage arm is divided into three parts: C_{12}, C_{1S}, and C_{2S}. Compared with the previous situation, C_{12} is significantly reduced. Additionally, because of the grounding of the shielding shell, C_{1S} has no impact on the gas state sensing unit. C_{2S} also acts as a coupling capacitor to ground. Now, the induced voltage on the gas state sensing unit can be determined using the following equation:

$$U_2 = \frac{U_1 C_{12}}{C_{12} + C_{2G} + C_{2S}}. \tag{8}$$

The comparison of (7) and (8) shows that the induced voltage on the gas state sensing unit is significantly reduced, and the designed shielding shell does make a difference.

Considering the remaining security risks and in conjunction with the shielding principle outlined above, an 80-mesh shielding mesh was chosen to be positioned above the flow-exchange hole to achieve a more comprehensive electric field shielding effect. The mesh size of the 80-mesh shielding mesh is 0.25 mm, and the wire thickness is only 0.1 mm, ensuring it would not seriously impede the gas commutation process. The material used for the shielding mesh is copper.

During the actual operation process, GIS will also suffer from operation and lightning overvoltage, with lightning overvoltage being the most serious. So, taking the 330-kV GIS which suffers from lightning overvoltage during its operation as an example, a 1:1 shielding mesh is incorporated in the simulation model. The simulation results indicate that the maximum induced voltage and electric field intensity of the sensing unit under various voltage levels of the GIS are both below 0.1 V and 60 V/m, respectively.

The expected induced voltage should not exceed 0.5 V and the withstand electric field intensity should not surpass 500 V/m. In practice, MEMS sensors can endure an overvoltage of approximately 2 V [38], with the least robust silicon material having a breakdown field intensity of 0.3 MV/cm.

C. Maximize the Flow-Exchange Hole

The flow-exchange hole affects the gas flow rate and sensor response time, so maximizing the hole as much as safely possible is crucial. The effect of the hole size on the sensing unit is investigated, and the 80-mesh grounded shielding mesh is kept intact over the flow-exchange hole during simulation. It can be found in Fig. 6(a) that enlarging the aperture increase induced voltage and electric field intensity on the sensing unit. Considering desired sensor safety requirements, a 2.5-mm hole size is ultimately chosen. The simulation results in Fig. 6(b) confirm that under this design, the maximum induced voltage and electric field strength on the sensing unit meet the safety criteria across various voltage levels of GIS.
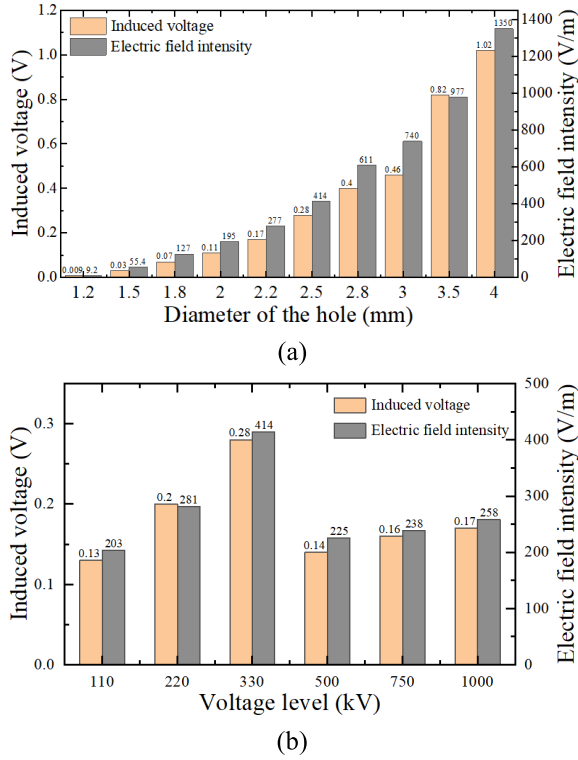
(a)

(b)

Fig. 6.   Maximum induced voltage and electric field intensity on the unit. (a) Effect of the hole size. (b) Final design.

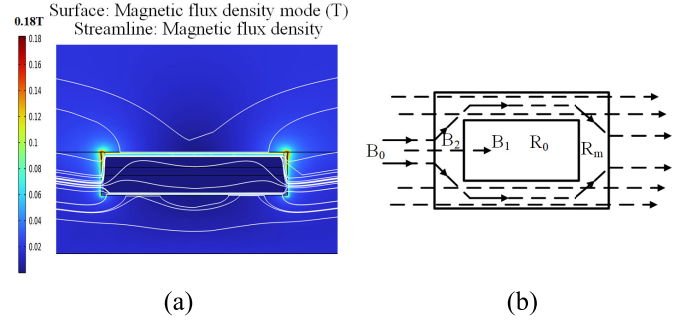(a)   (b)

Fig. 7.   Magnetic field shielding effect. (a) Simulation result. (b) Equivalent magnetic circuit model.

Fig. 8.   Sensitivity curves of the composite sensor and reference sensor.

D. Design of the Magnetic Field Shielding

In the analysis of Fig. 4, the magnetic field line is predominantly parallel to the gas state sensing unit, and the maximum magnetic induction intensity around it is 8.26×10^{-3} T. The magnetic field intensity acting upon the sensing unit is on the order of 10^{-4}, and the dimensions of the sensing unit are in the order of millimeters. Its internal loop forms a small area, and the angle between the magnetic field and the sensing unit is also quite small. Furthermore, the power frequency current operates at a frequency of 50 Hz. In summary, in accordance with Faraday's law of electromagnetic induction, the calculated induced electromotive force is essentially negligible, which will have minimal impact on the sensing unit. The rated current of GIS at different voltage levels does not significantly differ, leading to the same conclusion.

To enhance the reliability of the gas state sensing unit, additional magnetic field shielding solutions have been implemented. An additional property, a high magnetic permeability, is added to the shielding shell. The results are shown in Fig. 7. Analyzing the field in Fig. 7(a), the majority of magnetic field lines surrounding the sensing unit are redirected through the shielded shell. The high permeability shell effectively traps the magnetic field, significantly reducing its impact on the gas state sensing unit. The magnetic induction within the internal sensing unit drops by an order of magnitude to 1.88×10^{-5} T. Analyzing from the perspective of the circuit in Fig. 7(b), the high permeability shell exhibits low reluctance, making it more likely for the magnetic path to follow areas with low reluctance. Consequently, the remaining magnetic field intensity at the sensing unit decreases significantly, providing effective shielding against the magnetic field.
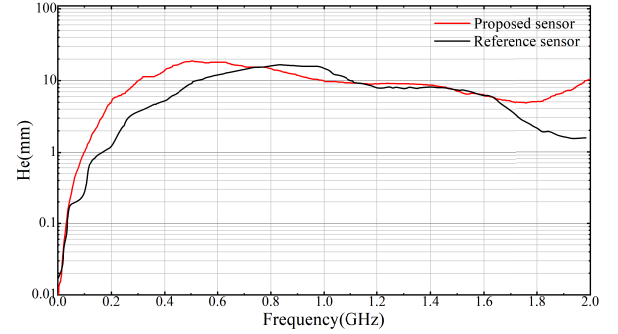
In summary, the high magnetic permeability and high conductivity of the grounded shielding shell design, along with the 80-mesh shielding mesh over the 2.5-mm flow-exchange hole, can satisfy the electromagnetic shielding requirements of the sensing unit. The material of the shielding shell is silicon steel, which has a magnetic permeability of 7600 H/m and an electrical conductivity of 2×10^6 S/m.

IV. EXPERIMENTATION AND VERIFICATION

A. UHF Performance of the Composite Sensor

Among the performance parameters of the UHF sensor, what we are most interested in is the amplitude of the output voltage under the same field strength environment, which is regarded as the output characteristic of the sensor, also called the sensitivity of the sensor. Therefore, in this article, the performance of the UHF sensor is evaluated using the sensitivity parameter He [39] according to the following equation:

$$\text{He}(f) = \frac{U(f)}{E(f)}. \tag{9}$$

The He of the composite sensor is measured in a standard gigahertz transverse electromagnetic (GTEM) chamber, which is a rectangular waveguide system [40]. The results of the red line in Fig. 8 reveal that the He is larger than 10 mm in most range of 0.3–1.5 GHz (the frequency range of PD UHF signals distribution, especially in 0.6–0.8 GHz), and the effective average sensitivity is as high as 13.3 mm, indicating that this is an excellent sensor for PD detection. In comparison, the sensitivity curve of an external UHF sensor [41] commonly used in the field is shown as the black line in Fig. 8, which calculates an effective average sensitivity of 10.5 mm.
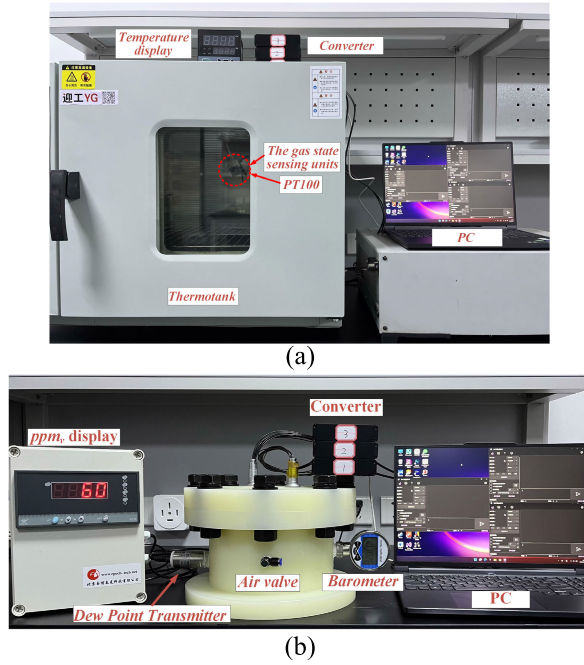
Fig. 9. Experimental setups. (a) For temperature. (b) For pressure and moisture.

TABLE II
ACCURACY AND MEASUREMENT RANGE OF THE STANDARD SENSORS

Sensor	Accuracy	Range
PT100	±0.1°C	-50~200°C
Barometer	±1Kpa	0~1MPa
Dew Point Transmitter (DMT143) [42]	1μL/L ± 20% of the reading	0~10000μL/L

B. Gas State Measurement Performance of the Composite Sensor

The volume of the composite sensor is relatively large, making it inconvenient to perform lateral comparisons between the sensors. Additionally, the shielding shell primarily affects the diffusion of moisture while having minimal impact on other state parameters. Therefore, a wide-range interval accuracy validation for the gas state sensing unit is conducted first, and several states are selected to verify the consistency of the composite sensor and the gas state sensing unit subsequently.

The experimental setups are shown in Fig. 9, where the setups in Fig. 9(a) for temperature validation and the setups in Fig. 9(b) for pressure and moisture validation. In the experiments, the measurement performance of the sensing unit is validated by comparing it with standard sensors, which are high-precision sensors or widely recognized sensor in the respective detection field. The accuracy and measurement range of the standard sensors are shown in Table II.

Fig. 10(a) and (b) shows the temperature and pressure error curves of three samples selected randomly. The results show that the temperature and pressure accuracy of the gas state sensing unit can reach ±0.2 °C in −20 °C–80 °C and ±3 kPa in 0.1–0.7 MPa, respectively, and there is a good measurement consistency among the three sensing units, which indicate that the design of the circuit does not affect the original accuracy of the two MEMS sensors.
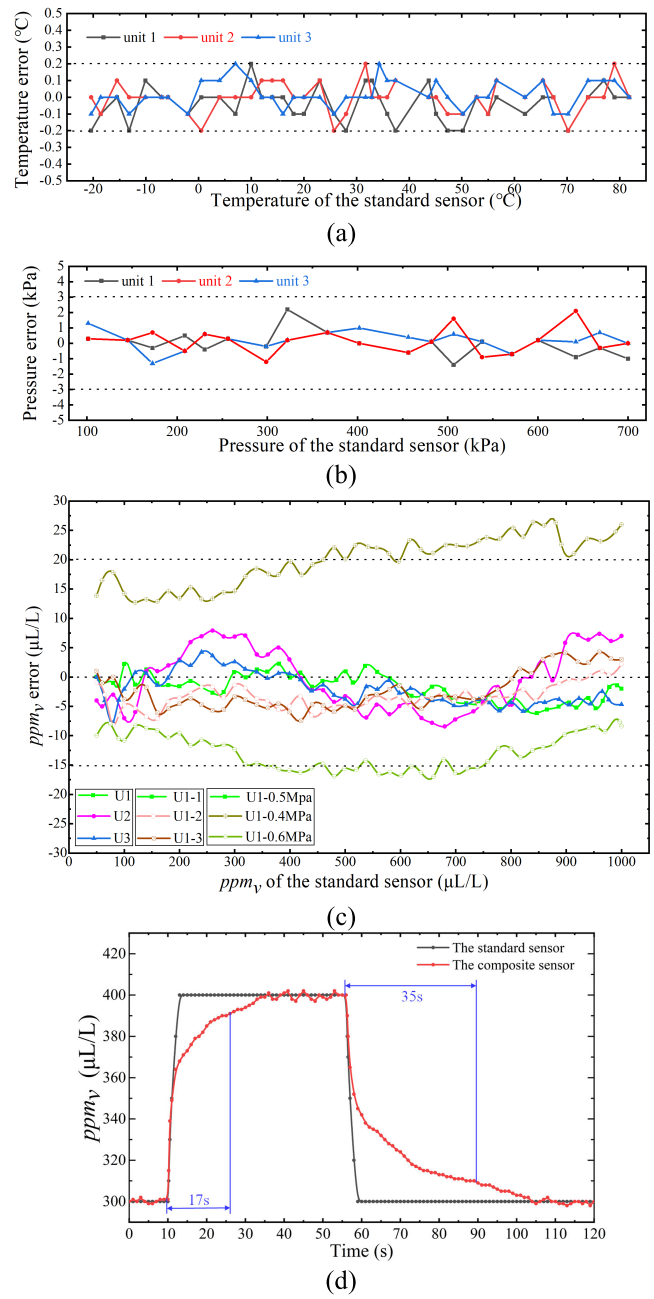
Fig. 10. Measurement performance. (a) Temperature. (b) Pressure. (c) Moisture. (d) Response and recovery time.

Fig. 10(c) shows the moisture error curves for the three sets of the experiments: a consistency experiment between the three sensing units, a repeatability experiment with three rounds of testing for a single sensor, and an error measurement experiment at different pressures. The results show that the sensor exhibits good consistency, high repeatability, and low error in the range of 0–1000 μL/L. Meanwhile, it can be found that the change in gas pressure causes an overall shift in the measurements, which is due to the fact that pressure has a much greater influence in moisture calculation in (4), but the measurement errors around the center value at different gas pressures are all within ±10 μL/L. Therefore, by adding a pressure-dependent correction factor to the program, the consistency of the ppm$_v$ measurements at different gas pressures

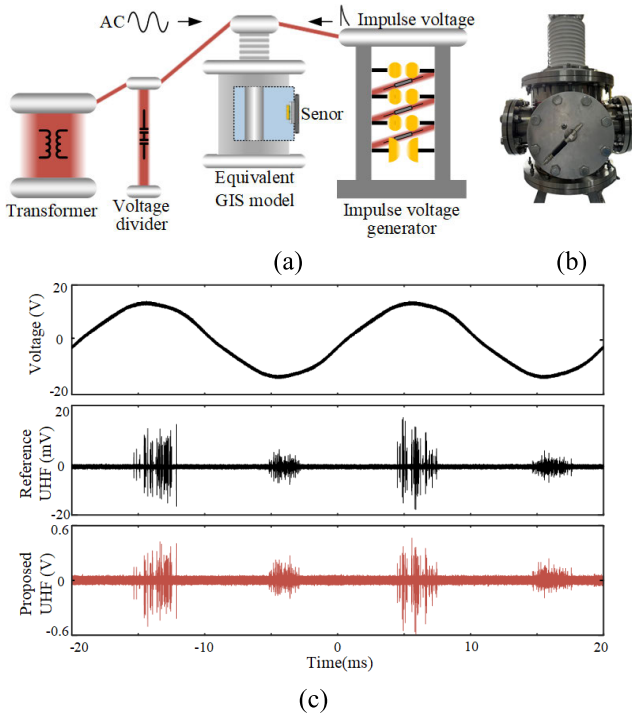Fig. 11. Safety verification and practical application. (a) Structure diagram of the experimental setup. (b) Physical map of the equivalent GIS model. (c) Outputs of the sensor.

TABLE III
PARAMETERS OF THE KEY EXPERIMENTAL COMPONENTS

Device	Parameters
High Voltage testing transformer without partial discharge	Rated capacity: 10kVA Rated secondary voltage: 100kV Rated frequency: 50Hz Partial discharge magnitude: $\leq$5pC
Voltage divider	Principle: coupling capacitor Maximum withstand voltage: 120kV Voltage division ratio: 1 : 1000
Equivalent GIS model	Diameter of the conductor: 80mm Inner diameter of the enclosure: 320mm
Impulse voltage generator	Principle: Marx circuit Number of levels: 3 Peak pulse voltage: 1100kV

TABLE IV
GAS STATE OUTPUT OF COMPOSITE SENSOR

Type	t	P	ρ	ppm_v	t_d	P_{20}	ppm_{v20}	t_{d1}
Standard	28.7	508.1		137				
Composite	28.8	507	31.2	141	-23.7	490	86	-39

can be achieved identically. The above analysis proves the feasibility of using MEMS sensors to measure RH to obtain low error ppm_v.

The measurement performance of the composite sensor is studied under several gas state. The results show that the composite sensor and the gas state sensing unit have high agreement in measurement accuracy, but the response time of the composite sensor is longer. The primary reason lies in the encapsulation of the gas state sensing unit within the composite sensor's shielding shell, and it senses the external gas through the flow-exchange hole. Both the dimensions of the flow-exchange hole and the shielding mesh have an impact on the water molecule's diffusion process. According to IEC 62271-203 [43], which stipulates that the moisture content of GIS gas chamber during normal operation should not exceed 500 μL/L, the transient response curve of the composite sensor for a step change in moisture content from 300 to 400 μL/L is tested. As shown in Fig. 10(d), the response time and recovery time stand at 17 and 35 s, respectively. Although these times might not be particularly brief, the composite sensor remains suitable for the GIS equipment, where the internal gas state changes extremely slowly.

C. Safety Verification and Practical Application

To validate the safety and practical measurement performance of the composite sensor, an experimental setup, as shown in Fig. 11(a), is constructed, and the parameters of the key components are shown in Table III. The composite sensor can be mounted on the flange of the equivalent model of a 220-kV GIS, where the power-frequency voltage, overvoltage, and current can be applied to the GIS model.

The experimental results demonstrate the composite sensor's stable operation under both normal GIS conditions and during exposure to overvoltage.

A needle defect is introduced inside the cavity of the GIS model to excite the PD signals, with gas pressure and trace moisture controlled at actual operational levels. Standard gas state measurement sensors are installed on the GIS model, and an external UHF sensor is placed at an observation window on the other side for reference. The parameters of the standard gas state measurement sensors are shown in Table II. The sensitivity curve of the reference UHF sensor is shown in Fig. 8. The experimental setups are located in the experimental hall with an outside temperature of 25.3 °C and RH of 41%. Voltage is gradually applied, and the outputs of the composite sensor are recorded, as illustrated in Fig. 11(c) and Table IV. The composite sensor achieves the detection of richer PD signals and the synchronous measurement of gas state parameters.

In summary, the developed sensor demonstrates excellent performance in UHF signals and gas state measurements, enabling secure synchronous detection of internal PD signals and gas state within the GIS on-site.

V. CONCLUSION

A novel composite sensor for UHF PD and gas state measurement in the GIS is proposed in the article. It is structured on a disk-type UHF sensor, enhanced with a gas state sensing unit. The gas state sensor is centered on two MEMS gas sensors, supplemented by components, such as MCU and EMC, which are capable of acquiring, processing, and transmitting gas state data. Through finite element simulation, the sensor's secure integration is achieved via a shielding shell made of silicon steel material and shielding mesh made of copper. Experimental validation confirms the sensor's safe operation post-integration. Furthermore, it exhibits better detection performance with an effective average UHF sensitivity of

13.3 mm and gas state measurement accuracy within ± 0.2 °C, ± 3 kPa, and ± 10 μL/L. Although the response and recovery times of the sensor are 17 and 35 s, respectively, they still adequately fulfill GIS detection requirements.

The proposed composite sensor can realize the simultaneous and safe detection of PD signals and gas state within GIS, facilitating a more comprehensive diagnosis of insulation defects. However, it is noteworthy that the results presented in this article are outcomes from short-term single measurements. During actual operation, the composite sensor will be in prolonged contact with gas, requiring further research on its compatibility with gas and the degradation of its performance during long-term service. Subsequent experiments will be conducted using this composite sensor to investigate these characteristics.

REFERENCES

[1] R. Bartnikas, "Partial discharges. Their mechanism, detection and measurement," *IEEE Trans. Dielectr. Electr. Insul.*, vol. 9, no. 5, pp. 763–808, Oct. 2002.

[2] J. Li, X. Han, Z. Liu, and Y. Li, "Review on partial discharge measurement technology of electrical equipment," *High Voltage Eng.*, vol. 41, no. 8, pp. 2583–2601, Aug. 2015.

[3] H. Song, Z. Zhang, J. Tian, G. Sheng, and X. Jiang, "Multiscale fusion simulation of the influence of temperature on the partial discharge signal of GIS insulation void defects," *IEEE Trans. Power Del.*, vol. 37, no. 2, pp. 1304–1314, Apr. 2022.

[4] K. Arikan, E. Önal, and Ş. Seker, "Time-frequency analysis of partial discharge current pulses in different gas environment under lightning impulse," *Meas. Sci. Rev.*, vol. 20, no. 4, 2020, pp. 196–201.

[5] T. N. Tran et al., "Dynamic measurement of surface discharge under different gaseous environments and pressures," in *Proc. Conf. Rec. IEEE Int. Symp. Elect. Insul.*, Vancouver, BC, Canada, Jun. 2008, pp. 424–427.

[6] X. Zhang, S. Xiao, J. Zhang, C. Li, Q. Dai, and Y. Han, "Influence of humidity on the decomposition products and insulating characteristics of CF3I," *IEEE Trans. Dielectr. Electr. Insul.*, vol. 23, no. 2, pp. 819–828, Apr. 2016.

[7] T. Hoshino, H. Koyama, S. Maruyama, and M. Hanai, "Comparison of sensitivity between UHF method and IEC 60270 for onsite calibration in various GIS," *IEEE Trans. Power Del.*, vol. 21, no. 4, pp. 1948–1953, Oct. 2006.

[8] X. Han, J. Li, L. Zhang, P. Pang, and S. Shen, "A novel PD detection technique for use in GIS based on a combination of UHF and optical sensors," *IEEE Trans. Instrum. Meas.*, vol. 68, no. 8, pp. 2890–2897, Aug. 2019.

[9] H. Wang, X. Zhang, X. Han, Y. Sun, H. Chen, and J. Li, "A novel composite sensor for overvoltage and UHF partial discharge measurement in GIS," *IEEE Trans. Power Del.*, vol. 37, no. 6, pp. 5476–5479, Dec. 2022.

[10] R. Huang, C. Gao, F. Zhou, G. Liu, Y. Huang, and J. Peng, "Key properties test and analysis of gas density monitor used for gas-insulated switchgear after long-term operation," in *Proc. IEEE Int. Conf. High Voltage Eng. Appl. (ICHVE)*, Beijing, China, Sep. 2020, pp. 1–4.

[11] D. H. Zhu, W. Yan, and K. Y. Tan, *State Monitoring and Fault Diagnosis Technology for Electrical Equipment*, vol. 3. Beijing, China: Electric Power Press, 2009, p. 23.

[12] X. Gu et al., "Development of a full temperature range calibrator for SF6 gas density monitors," *High Voltage Appl.*, vol. 51, no. 1, pp. 127–132, Jan. 2015.

[13] X. Y. Shi, W. Zha, F. Sun, X. H. Wang, and Q. G. Zhang, "Inner temperature distribution of UHV GIS using infrared thermal diagnosis technology," *High Voltage Eng.*, vol. 33, no. 6, pp. 16–20, 2007.

[14] M. Yu-long, L. Chen, Y. Qiang, T. Ju, and Z. Fu-ping, "Contact temperature monitoring and layout optimization of shell temperature sensor of 500 kV GIS," in *Proc. IEEE Int. Conf. High Voltage Eng. Appl. (ICHVE)*, Beijing, China, Sep. 2020, pp. 1–4.

[15] W. Wei, L. Zhang, J. Chen, T. Zhao, L. Zou, and D. Chu, "Monitoring of GIS contact temperature based on surface acoustic wave technology and ZigBee network," in *Proc. 14th IEEE Conf. Ind. Electron. Appl. (ICIEA)*, Xi'an, China, Jun. 2019, pp. 1437–1441.

[16] D. Lu et al., "The effect of the dew point instrument on SF6 gas humidity field testing," *Electr. Switchgear*, vol. 52, no. 6, pp. 87–89, Jul. 2014.

[17] T. Islam, A. U. Khan, J. Akhtar, and M. Z. U. Rahman, "A digital hygrometer for trace moisture measurement," *IEEE Trans. Ind. Electron.*, vol. 61, no. 10, pp. 5599–5605, Oct. 2014.

[18] Z. H. Zargar, K. J. Akram, G. R. Biswal, and T. Islam, "A linear capacitive sensor for ppm moisture measurement in SF6 gas-insulated switchgear," *IEEE Trans. Instrum. Meas.*, vol. 70, pp. 1–8, 2021.

[19] Y. Tang, "Research and application of an online monitoring system on moisture in GIS," M.S. thesis, Dept. Electron. Eng., Zhejiang Univ., Zhejiang, China, 2015.

[20] M. Porus, Th. A. Paul, and A. Kramer, "Application of a multi-parameter sensor system for monitoring dielectric insulation of gas mixtures," *IEEE Trans. Dielectr. Electr. Insul.*, vol. 24, no. 2, pp. 847–851, Apr. 2017.

[21] L. Graber, "Improving the accuracy of SF6 leakage detection for high voltage switchgear," *IEEE Trans. Dielectr. Electr. Insul.*, vol. 18, no. 6, pp. 1835–1846, Dec. 2011.

[22] P. Cheetham and A. Hellany, "Density monitoring of high-voltage SF6 circuit breakers," in *Proc. IEEE Elect. Insul. Conf. (EIC)*, Philadelphia, PA, USA, Jun. 2014, pp. 92–96.

[23] H. Zhou et al., "Optical sensing in condition monitoring of gas insulated apparatus: A review," *High Voltage*, vol. 4, no. 4, pp. 259–270, Nov. 2019.

[24] J. Li, X. Han, Z. Liu, and X. Yao, "A novel GIS partial discharge detection sensor with integrated optical and UHF methods," *IEEE Trans. Power Del.*, vol. 33, no. 4, pp. 2047–2049, Aug. 2018.

[25] Z. Shiling, "On-line monitoring study for high voltage GIS HF gas by flange-type optical fiber sensing," in *Proc. Asia Commun. Photon. Conf. (ACP)*, Hangzhou, China, Oct. 2018, pp. 1–3.

[26] Y. Tong, Y. Wu, B. Liu, and J. Shen, "The optimal design of electromagnetic compatibility for electronic transformer," in *Proc. Int. Conf. Power Syst. Technol. (POWERCON)*, Guangzhou, China, Nov. 2018, pp. 1037–1042.

[27] M. Cho, J.-G. Lee, and R.-E. Kim, "Design of shield ring for UHV-class gas-insulated switchgear spacer with built-in Rogowski coil based on electromagnetic interference analysis," in *Proc. 6th Int. Conf. Electric Power Equip.-Switching Technol. (ICEPE-ST)*, Seoul, South Korea, Mar. 2022, pp. 312–316.

[28] M. I. A. Asri et al., "MEMS gas sensors: A review," *IEEE Sensors J.*, vol. 21, no. 17, pp. 18381–18397, Sep. 2021.

[29] T. Choudhury and G. R. Biswal, "SF6 density-and-viscosity sensing in gas insulated switchgear using MEMS resonator," in *Proc. IEEE 1st Int. Conf. Power Electron., Intell. Control Energy Syst. (ICPEICES)*, Delhi, India, Jul. 2016, pp. 1–6.

[30] G. R. Biswal, T. Choudhury, T. Islam, S. C. Mukhopadhyay, and V. Vashisht, "Design and modeling of MEMS-based trace-level moisture measurement system for GIS applications in smart grid environment," *IEEE Sensors J.*, vol. 17, no. 23, pp. 7758–7766, Dec. 2017.

[31] H. Chen, H. Wang, Y. Gao, X. Han, and J. Li, "Study on the temperature distribution characteristics of SF6 gas in GIS based on multi-physical field coupling," in *Proc. IEEE 4th Int. Conf. Elect. Mater. Power Equip. (ICEMPE)*, Shanghai, China, May 2023, pp. 1–4.

[32] R. Song et al., "Assessment of gas insulation state in GIS equipment based on relevance vector machine," *High Voltage Appl.*, vol. 52, no. 12, pp. 237–243, Dec. 2016.

[33] *Datasheet-STM32F103x8*, STlife.augmented, Cham, Switzerland, Sep. 2023.

[34] *IEEE Guide for Moisture Measurement and Control in SF6 Gas-Insulated Equipment*, Standard IEEE C37.122.5, 2013.

[35] International Association for the Properties of Water and Steam, *Revised Release on the IAPWS Industrial Formulation 1997 for the Thermodynamic Properties of Water and Steam*, IAPWS Secretariat, Luzern, Swiss Confederation, 2007.

[36] J. Liu et al., "Error analysis of SF6 density relay in pressure monitoring of GIS chamber," *Zhejiang Electr. Power*, vol. 41, no. 2, pp. 73–77, Sep. 2021.

[37] J. Wang, "Influence factors and revision methods of GIS SF6 humidity monitoring," *Hebei Electr. Power*, vol. 29, no. 1, pp. 28–29, 2010.

[38] *Sensirion Humidity Sensors SHT3x Datasheet digital*, Sensirion, Cham, Switzerland, Oct. 2015.

[39] Y. Jia et al., "Performance comparison of typical built-in UHF sensors used for GIS PD detection," *Appl. Mech. Mater.*, vols. 672–674, pp. 1143–1150, Oct. 2014.

[40] M. D. Judd and O. Farish, "A pulsed GTEM system for UHF sensor calibration," *IEEE Trans. Instrum. Meas.*, vol. 47, no. 4, pp. 875–880, Aug. 1998.

[41] *External UHF Partial Discharge Sensor (WFS-D8-UHF-E) Product Specification*, Winfoss Seeker, Beijing, China, Apr. 2022.

[42] *DMT143 Dew Point Transmitter Datasheet B211207Zh-J*, Vaisala, Suomi, Finland, 2022.

[43] *High-Voltage Switchgear and Controlgear—Part 203: AC Gas-Insulated Metal-Enclosed Switchgear for Rated Voltages Above 52 kV*, Standard IEC 62271-203 Ed.3.0, 2022.

Ruochen Guo (Member, IEEE) was born in Shandong, China, in 1994. He received the Ph.D. degree in electrical engineering with Xi'an Jiaotong University, Xi'an, China, in 2022.

From 2021 to 2022, he was a Joint Ph.D. Student in the area of applied physics in electrotechnology with the KTH Royal Institute of Technology, Stockholm, Sweden. He is currently a Researcher with the High Voltage Technology Group, Electrical Sustainable Energy Department, Delft University of Technology, Delft, The Netherlands.

Huan Chen was born in Nanyang, Henan, China, in 1999. He received the B.Sc. degree in electrical engineering from the China University of Petroleum (East China), Qingdao, China, in 2021. He is currently pursuing the Ph.D. degree with Xi'an Jiaotong University, Xi'an, China, with a focus on detective techniques of gas state for gas-insulated switchgear equipment.
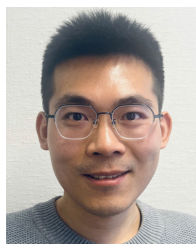
Xutao Han was born in Xi'an, Shaanxi, China, in 1991. He received the B.Sc. and Ph.D. degrees in electrical engineering from Xi'an Jiaotong University, Xi'an, in 2013 and 2019, respectively.

He is currently a Research Assistant with Xi'an Jiaotong University, with a focus on the detective and diagnostic techniques for gas-insulated switchgear equipment.

Haotian Wang was born in Xi'an, Shaanxi, China, in 1999. He received the B.Sc. degree in electrical engineering from Xi'an Jiaotong University, Xi'an, in 2020, where he is currently pursuing the Ph.D. degree with a focus on the fault detection and state evaluation for gas-insulated switchgear equipment.

Xuanrui Zhang was born in Zhengzhou, Henan, China, in 1994. He received the Ph.D. degree from Xi'an Jiaotong University, Xi'an, China, in 2023.

He is currently an Assistant Professor with Xi'an Jiaotong University. He focuses on the partial discharge detection and impulse test technology for power transformers.

Zhaoyu Zhang was born in Yuncheng, Shanxi, China, in 1995. He received the M.S. degree in electrical engineering from Xi'an Jiaotong University, Xi'an, China, in 2020. He is currently pursuing the double Ph.D. degree in electrical engineering with Xi'an Jiaotong University, and Politecnico di Torino, Turin, Italy.

His main fields of interest are the intelligent sensing technology, fault detection, and state evaluation for power equipment.

Junhao Li (Senior Member, IEEE) was born in Xuchang, Henan, China, in 1980. He received the Ph.D. degree in electrical engineering from Xi'an Jiaotong University, Xi'an, China, in 2010.

He is currently a Professor with Xi'an Jiaotong University, where he is involved in the detective and diagnostic techniques for electrical equipment and new types of the test method for electrical equipment.